

## Article

# Erosion Monitoring in Benggang Based on Control-Free Images and Nap-of-the-Object Photogrammetry Techniques

Linting Zhong, Jianfeng Lai, Guangxi Lai, Xiang Ji, Yue Zhang, Fangshi Jiang  Yanhe Huang and Jinshi Lin \*

College of Resources and Environment, Fujian Agriculture and Forestry University, Fuzhou 350002, China; lintingzhong0110@163.com (L.Z.); holmesl@163.com (J.L.); 18806089007@163.com (G.L.); jixiangss@126.com (X.J.); zhangyue@fafu.edu.cn (Y.Z.); jfsfafu@163.com (F.J.); yanhehuang@163.com (Y.H.)

\* Correspondence: jslin@fafu.edu.cn; Tel.: +86-180-8472-5185

**Abstract:** Unmanned aerial vehicle (UAV)-based nap-of-the-object photogrammetry techniques can be utilized to periodically monitor the erosion of nearly vertical cliffs. However, the broader applicability of such techniques is hindered by the necessity of deploying multiple ground control points around collapsing walls. This study aims to accurately assess Benggang erosion before and after the rainy season by analyzing the optimal flight proximity distance using close-range photogrammetric techniques. The assessment centers on positioning accuracy, point cloud data, and digital surface model (DSM) data. Nap-of-the-object photogrammetry techniques are integrated with control-free image methods to conduct aerial surveys of Benggang, generating high-resolution three-dimensional (3D) DSMs. The feasibility of this control-free-image-based nap-of-the-object photogrammetry technique is evaluated based on positioning accuracy and measurement errors, comparing the generated DSMs with real-time kinematic (RTK) measured coordinate data. The results indicate that a flight proximity distance of 20 m is optimal for obtaining data in the Benggang area using control-free-image-based nap-of-the-object photogrammetry. This scheme yields an average reprojection error of approximately 0.01 pixels in data processing before and after rainfall, showing strong consistency in the spatial distribution of the two-stage 3D models. The mean absolute error in planar accuracy is between 0.01 m and 0.02 m, and that in elevation accuracy is approximately 0.03 m, with the lowest errors reaching the millimeter level. Therefore, control-free images combined with nap-of-the-object photogrammetry techniques can meet relevant demands for monitoring landslide erosional areas, providing technical support for extensive, safe, and efficient Benggang erosion monitoring.



**Citation:** Zhong, L.; Lai, J.; Lai, G.; Ji, X.; Zhang, Y.; Jiang, F.; Huang, Y.; Lin, J. Erosion Monitoring in Benggang Based on Control-Free Images and Nap-of-the-Object Photogrammetry Techniques. *Appl. Sci.* **2024**, *14*, 2112. <https://doi.org/10.3390/app14052112>

Academic Editor: Yangquan Chen

Received: 3 February 2024

Revised: 20 February 2024

Accepted: 1 March 2024

Published: 4 March 2024



**Copyright:** © 2024 by the authors. Licensee MDPI, Basel, Switzerland. This article is an open access article distributed under the terms and conditions of the Creative Commons Attribution (CC BY) license (<https://creativecommons.org/licenses/by/4.0/>).

## 1. Introduction

Benggang, a unique erosional landform type in the red soil area of southern China, is formed by the decomposition, accumulation, and erosion of soil or rock weathering shells on hillsides caused by hydraulic force and gravity [1–4]. Anthropogenic activities are important factors in the formation of Benggang, the impact of which is secondary only to debris flow. Benggang poses threats such as land resource destruction, sediment deposition in river channels and farmlands, ecological deterioration, various other ecological issues, and significant harm to people's lives and livelihoods [5,6]. In the Benggang erosion process, the Benggang wall is a key link influencing the occurrence and progression of erosion. It is crucial to conduct intensive, long-term observation in typical Benggang areas [7]. However, the unique and complex topographic characteristics of Benggang make these areas difficult to monitor in real time or over large scales using traditional methods and manual surveys. The convenient, safe, and efficient monitoring of Benggang walls in these areas is critical in order to safeguard them from dangerous levels of erosion.

In recent years, unmanned aerial vehicle (UAV) photogrammetry applications have expanded across various industries [8–12]. Researchers have explored soil erosion using

oblique photogrammetry and ground control points to monitor Benggang areas dynamically. Jiang et al. [13] used UAV tilt photography for this purpose, analyzing spatial changes in Benggang. Zhou et al. [14] used UAV oblique photogrammetry to monitor changes in erosion and to extract comprehensive terrain information. However, steep collapse walls and significant drops [15] render oblique photogrammetry inapplicable due to the limited angles of overlooking imaging, particularly in monitoring collapse wall erosion. It is important to address these limitations and enhance accuracy in capturing surface details of nearly vertical collapse walls [16–19].

The Zuxun Zhang Academician team of Wuhan University launched nap-of-the-object photography [17,18] using UAVs close to the research surface for image data acquisition, thus obtaining subcentimeter high-resolution images [19]. Through the further processing of photogrammetry software, the accurate coordinates and point cloud model of the study area are obtained, and the fine model is generated. At present, this technology has been used in Benggang erosion monitoring. Researchers like Li et al. [16] have utilized nap-of-the-object photogrammetry as an alternative to oblique photogrammetry, reducing the measurement error by up to 45.45% and improving overall elevation accuracy by 162.5%. Nap-of-the-object photogrammetry technology can be used to extract erosional geomorphology features in Benggang areas efficiently and accurately.

However, it is necessary to establish multiple control points on a steep collapse wall to accurately determine Benggang topography and erosional information. The complexity and precariousness of Benggang areas make this method perilous and challenging to use, particularly at larger scales, under typical field conditions.

The development of control-free-image-based photogrammetry technology is essential to monitoring Benggang erosion. This technology has been applied successfully in various other fields. Li et al. [20], for instance, demonstrated its utility by employing no control points, integrating auxiliary data recorded by UAV systems, and performing fast UAV image mosaic and correction. Zhao et al. [21] improved orthophoto image accuracy without ground control points (GCPs) or high-precision sensors. He et al. [22] investigated photogrammetric methods for UAVs without GCPs, comparing them with the traditional approach and verifying their effectiveness in estimating barge inventories in dynamic environments. Li et al. [23] used low-cost micro-drones and structure-from-motion (SFM) photogrammetry to measure paleo-seismic offsets without GCPs. Maier et al. [24] generated an automatic snow depth map without relying on GCPs. There have been several other valuable contributions to this area. Zhou et al. [25] obtained and processed data for a landslide-debris flow disaster model using control-free UAV photogrammetry images and quickly determined landslide shape characteristics, debris flow channel characteristics, and other related parameters from the aerial survey date. Wu et al. [26] used UAV technology to conduct large-scale aerial surveys of islands and reefs without control points. UAV-based control-free image technology can significantly enhance efficiency without necessitating pre-set control points while ensuring sufficient accuracy, which may make it a highly effective approach to monitoring complex terrain changes [21,27]. However, there have been few studies on the application of this technology in Benggang erosion monitoring.

To address this research gap, Tongluo Mountain Benggang in Yangkeng Village, Longmen Town, Anxi County, was utilized as a case study area. UAV images were obtained at various flight proximities; then, the optimal distance was determined in terms of positioning accuracy, point cloud data, and DSM data direction. Control-free nap-of-the-object photogrammetry image technology was combined with this optimal flight proximity to adjust the photogrammetric route and lens head of the point cloud model in the study area. The shooting plane of the route parallel to the Benggang was fitted in order to obtain fine image data. The feasibility of this approach was verified by comparing aerial survey data with image control points and ground real-time kinematic (RTK) base station measurement data. The findings may provide technical support for the efficient and accurate monitoring of collapse walls.

## 2. Materials and Methods

### 2.1. Overview of Study Area

The study area is located in Yangkeng Village, Longmen Town, south of Anxi County, Fujian Province, as depicted in Figure 1. It is characterized by a south subtropical maritime monsoon climate, with an annual average temperature of 20.3 °C and an average annual precipitation of 1600 mm mainly occurring from March to September. The annual average relative humidity is 77%; the annual average sunshine hours total approximately 2000; and the frost-free period is 350 days. It is a typical area of granite Benggang development in the south of China [16]. Benggang and gullies in the study area have both vertical and horizontal orientations, with serious erosion and sparse vegetation.

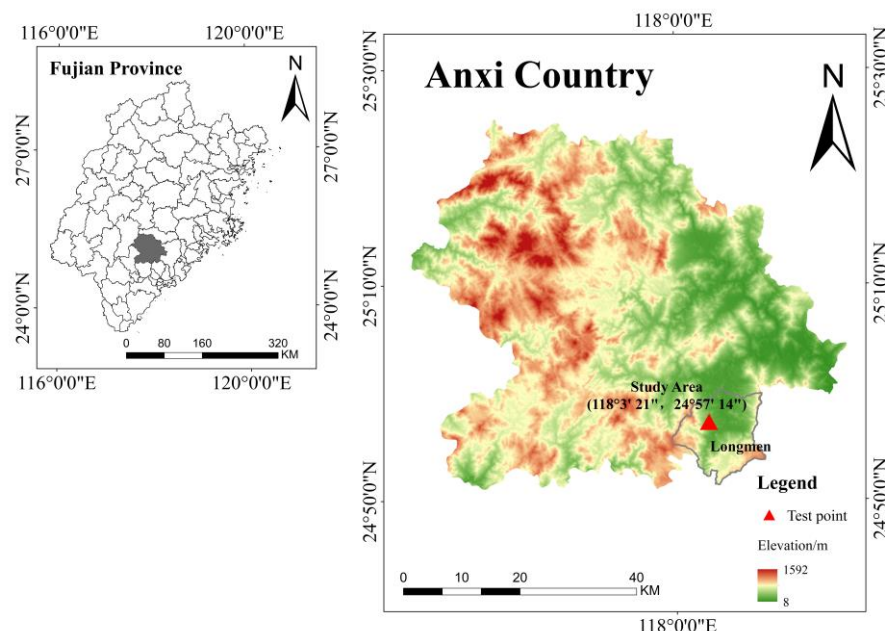


**Figure 1.** Benggang study area.

### 2.2. Data Acquisition

#### 2.2.1. Layout and Acquisition of Ground Checkpoints

Ground checkpoints were deployed in the study area with reference to the optimal ground checkpoint deployment scheme, characterized by a small number of evenly spaced intermediate points around the perimeter and parallel to the flight path [28,29]. A total of 10 ground checkpoints were deployed at the top, middle, and bottom of the Benggang, respectively. Unfortunately, the ground checkpoint situated in the middle of the bottom part of the Benggang was lost during the second test due to rainfall, resulting in 9 ground checkpoints remaining for subsequent analysis. To ensure consistency with UAV image position and orientation system (POS) data and the coordinate system of the ground checkpoints, the coordinates of the study area were kept in alignment with the WGS-1984-UTM-50N projected coordinate system.

The Trimble R2 GPS (Westminster, CO, USA), operating in RTK network CORS mode, was employed to measure the coordinates of each ground checkpoint with an accuracy of  $\pm 10$  mm + 1 ppmRMS horizontally and  $\pm 20$  mm + 1 ppmRMS vertically. Ground checkpoints were established in the study area prior to UAV imagery collection, and the Trimble R2 GPS was used to measure the coordinates of each ground checkpoint in RTK network CORS mode. Each ground checkpoint was measured twice, with the difference between the coordinates of the two measured planes not exceeding 2 cm. Simultaneous measurements of the elevation and plane were taken for the ground checkpoints, with elevation points being measured twice, ensuring that the difference between geodesic heights in each measurement was no more than 2 cm. The acquisition parameters included

observation time of 1; sampling interval of 1 s; observation calendar of 10"; and RTK network CORS mode acquisition operation, targeting ground checkpoint data. The average of the two measurement results served as a reference to verify the accuracy of final control-free nap-of-the-object photogrammetry images. The layout of ground checkpoints, GCPs, and ground checkpoint data acquisition in the study area are illustrated in Figure 2.

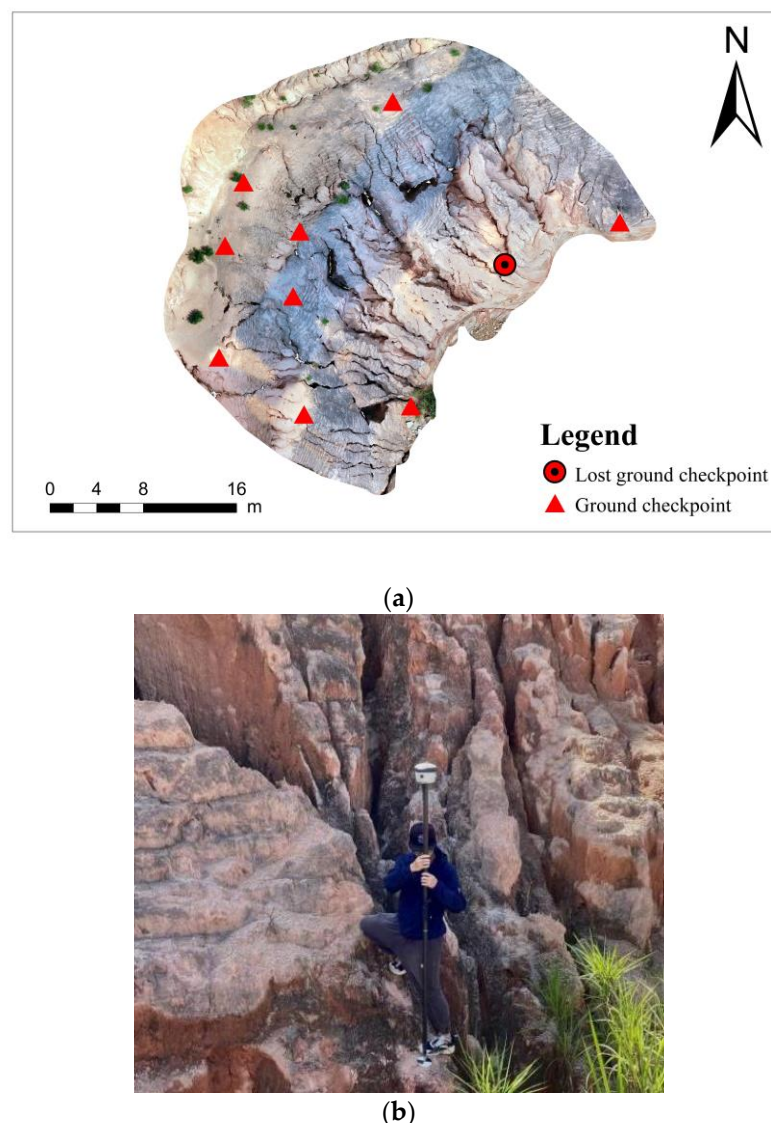


**Figure 2.** (a) Ground checkpoint deployment map; (b) Trimble R2 GPS Survey Target ground checkpoints.

#### 2.2.2. UAV Data Image Acquisition

##### Data Acquisition at Different Flight Approximation Distances

The flight proximity of the UAV was set to 15 m, 20 m, 25 m, or 30 m in this study in accordance with the characteristics of the study area. UAV image data were collected with nap-of-the-object photogrammetry, and another flight proximity of 10 m was utilized to create an experimental control group, as shown in Figure 3. To ensure consistent elevation data throughout the entire monitoring process, we set up the most available route plan [30]. A uniform arrangement was adopted around the study area based on the optimal image control point layout, and a small number of internal control points was implemented [28,29], with 9 GCPs being positioned in the study area as shown in Figure 4.

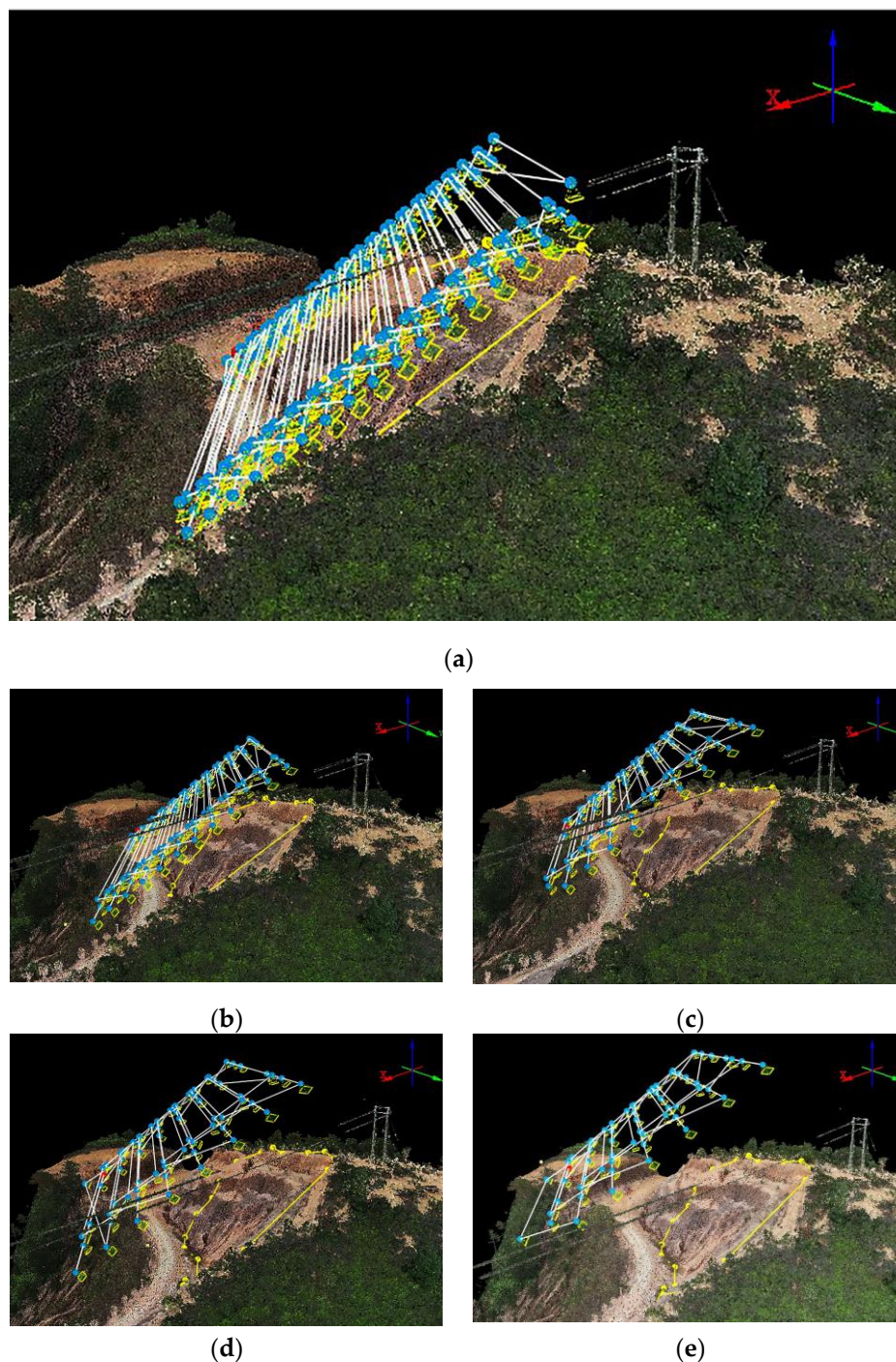


**Figure 3.** Distance course scenarios. (a) 10 m (control); (b) 15 m; (c) 20 m; (d) 25 m; (e) 30 m.

#### Control-Free-Image-Based Nap-of-the-Object Photogrammetry Data Acquisition

Two nap-of-the-object photogrammetry techniques, one based on image control and one based on control-free images, were used to gather imagery for the study area. The flight altitude was set to 40 m; the overlap rate of the heading image, to 80%; and the overlap rate of the side image, to 70%. The lenses were all tilted at a  $45^\circ$  angle with respect to the route for data acquisition. The oblique photography point cloud model collected by nap-of-the-object photogrammetry was used to plan the flight path in the study area, as shown in Figure 5. The flight parameters were set using DPGO 22.03.01 software. The course image overlap rate was 80%, and the side image overlap rate was 70% [31–33]. The optimal flight proximity was determined as shown in Figure 6.

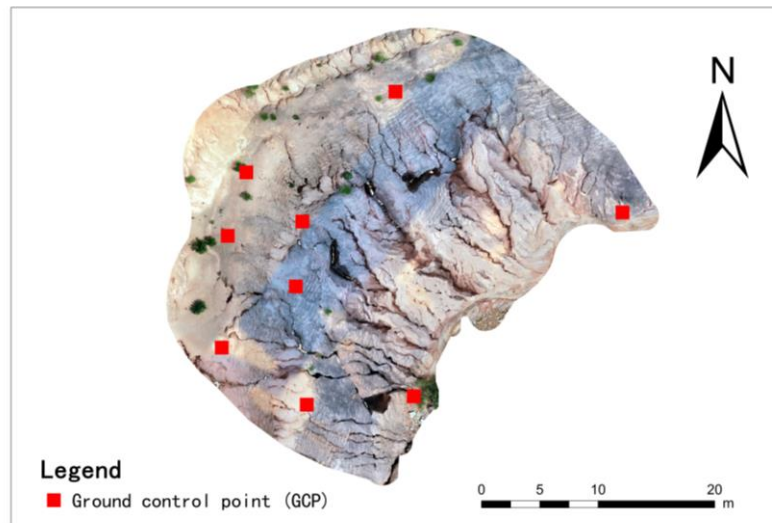


**Figure 4.** Ground control point (GCP) distribution map.

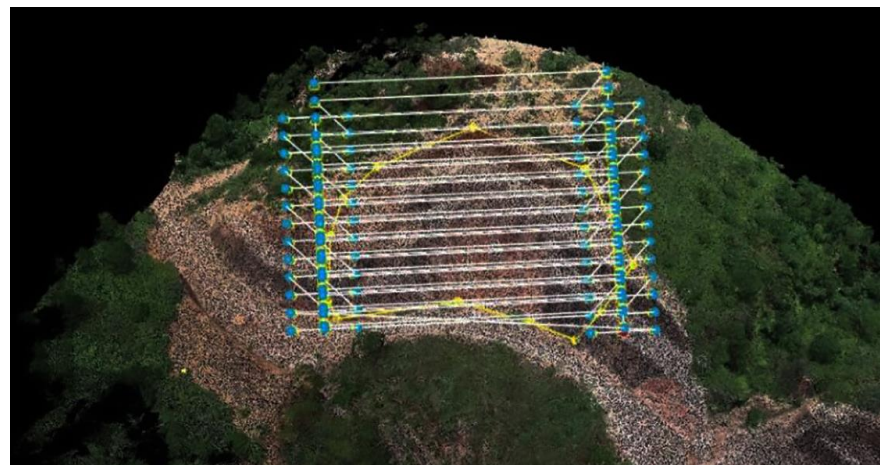


**Figure 5.** UAV flight routes.

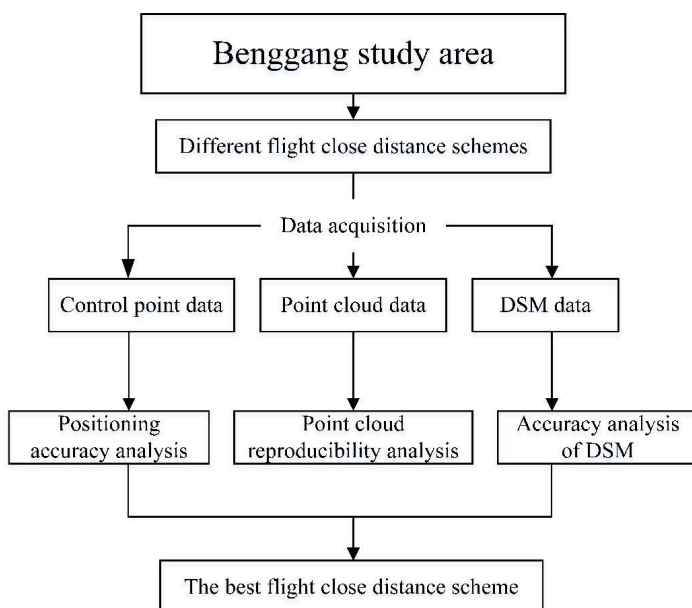


**Figure 6.** The best technical route for flight close distance acquisition.

Image data for the study area were gathered on 22 June 2022 and on 15 July 2022. The images were taken in the morning under clear weather conditions with minimal wind. Notably, rainfall occurred between these two image collection periods, with a 23-day interval between them. An RG3-M (Cape Cod, MA, USA) rainfall recorder was installed to confirm the presence of substantial rainfall in the study area on both image collection days. The DJI Phantom 4RTK UAV (Shenzhen, China) was selected, equipped with an autofocus FC6310R camera and a 1-inch 2000-megapixel image sensor. The remote control included a built-in GS RTK App for intelligent route planning to control the UAV data collection process. The parameters of the UAV and camera are described in Table 1.

**Table 1.** Basic parameters of UAV and camera.

DJI Phantom 4 RTK UAV		Basic Parameters of Camera	
Parameter	Value	Parameter	Value
Weight (g)	1391	Sensors (in)	1
Wheelbase (mm)	350	Effective pixels	20 million
Maximum flight speed (km/h)	50	Resolution (mm)	5472 × 3648
Maximum tilt angle (°)	25	Aperture	f 2.8–f 11
Maximum wind speed (m/s)	10	Focal length (mm)	8.8
Maximum flight time (min)	30	Equivalent focal length (mm)	24
Vision system	Five-way obstacle avoidance	Focusing distance (m)	1 m–∞

### 2.3. Research Methodology

UAV image data were obtained using nap-of-the-object photogrammetry technology. The aerial survey data were aerial triangulation encryption with DJI Terra 3.4.4 software to generate fine 3D models and point cloud data. The coordinate data collected from orthophoto image Digital Orthophoto Map (DOM), point cloud data, and the digital surface model (DSM) were utilized as reference values. ArcMAP 10.2 and DJI Terra software were utilized to evaluate the accuracy of the measurement results and determine the optimal flight proximity in the Benggang study area [23,24]. A comparison was made with data obtained using image control nap-of-the-object photogrammetry, with measured RTK coordinate data as a reference. The error source of the 3D model was analyzed; then, the feasibility of control-free-image-based nap-of-the-object photogrammetry in analyzing erosion and collapse walls was investigated, as depicted in Figure 7.

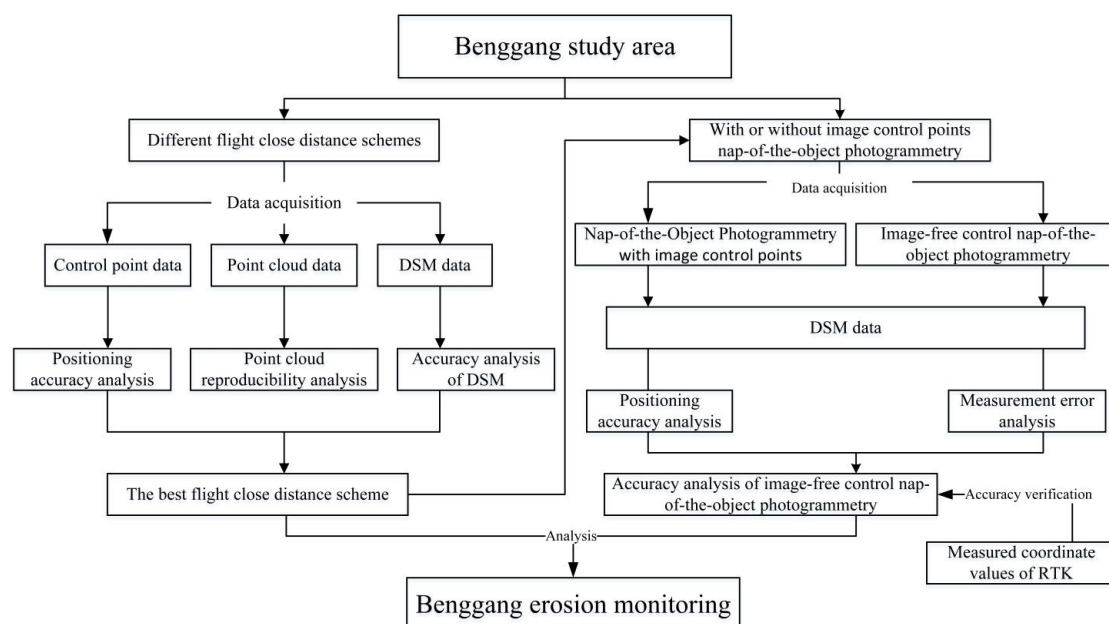


**Figure 7.** Workflow of research.

## 2.4. Data Processing

### 2.4.1. UAV Data Processing

#### (1) Point Cloud and DSM Data

The coordinates of UAV images and GCPs (checkpoints) were imported into DJI Terra 3.4.4 software. Ground control points were marked in the images; then, point cloud and DSM data were generated through calculation of aerial triangulation, 2D reconstruction and 3D reconstruction.

#### (2) DSM Volume Difference Calculation

The acquired DSM data were imported into ArcGIS 10.2 software, followed by fill and excavation analysis in the software's 3D Analyst Tools. The DSM data generated under different flight proximity conditions were superimposed with the DSM data for the control group to analyze differences in terms of volume changes.

#### (3) Point Cloud Data Index Calculation

The acquired point cloud data were imported into Point Cloud Magic V2.0 (PCM V2.0) and Cloud Compare 2.12 software to denoise the point cloud and crop the main study area, superimpose the point cloud of the cropped main study area, and calculate the distance from point cloud to point cloud.

### 2.4.2. Data Processing for Model Coordinate Extraction

DJI Terra 3.4.4 software was used to process the generated DOM image data and DSM data, which were analyzed in ArcGIS 10.2 with 10 ground checkpoints for coordinate data extraction. The coordinates were extracted by adding the point file, ensuring that the coordinate system and DOM image coordinates were consistent. Spatial analysis was then performed on the 10 ground checkpoints to extract points and obtain elevation values. Subsequently, data management tools were employed to add X-coordinate and Y-coordinate values, ultimately outputting the coordinates of the 10 ground checkpoints. The checkpoint coordinates were successfully extracted, as discussed in detail below.

### 2.4.3. Analysis of Control-Free-Image Accuracy

To explore the feasibility of control-free-image-based nap-of-the-object photogrammetry in monitoring Benggang, 10 ground checkpoints were installed parallel to the course within the Benggang study area. The coordinates were collected through the RTK network's CORD mode, then compared with measured coordinate values extracted from the UAV images for the corresponding ground checkpoints. As per Formula (1), the horizontal X-coordinate error of the GCP can be expressed as  $\Delta x$ ; the horizontal Y-coordinate error, as  $\Delta y$ ; the elevation Z error, as  $\Delta z$ ; and the planar direction X Y error, as  $\Delta xy$ . The measured coordinates of the ground checkpoint are denoted by M ( $x_i, y_i, z_i$ ), and the computed coordinates of the ground checkpoint are denoted by C ( $x'_i, y'_i, z'_i$ ).

The planar and elevation coordinates, labeled similarly, were obtained through nap-of-the-object photogrammetry acquisition as DOM image data and DSM data and were then extracted through ArcMAP software to create a model corresponding to the measured coordinate points, which were calculated as 3D coordinates (X, Y, Z) coordinate data. Formula (2) was used to determine the root mean square error (RMSE), or "medium error", of the GCP position. Measurement accuracy was then defined according to the error data from the DOM image and DSM.

$$\Delta x = x_i - x'_i; \Delta y = y_i - y'_i; \Delta z = z_i - z'_i; \Delta xy = \sqrt{(x_i - x'_i)^2 + (y_i - y'_i)^2} \quad (1)$$

$$M_x = \pm \sqrt{\sum_{i=1}^n (\Delta x \Delta x)/n}; M_y = \pm \sqrt{\sum_{i=1}^n (\Delta y \Delta y)/n}; M_z = \pm \sqrt{\sum_{i=1}^n (\Delta z \Delta z)/n}; M_{xy} = \pm \sqrt{\sum_{i=1}^n (\Delta xy \Delta xy)/n} \quad (2)$$

where  $M_x$ ,  $M_y$ ,  $M_z$ , and  $M_{xy}$  represent the RMSE of the ground checkpoints in m;  $\Delta_x$ ,  $\Delta_y$ ,  $\Delta_z$ , and  $\Delta_{xy}$  represent the discrepancy between the field measurement value and the extracted

value of the ground checkpoints in m; and n represents the number of ground checkpoints used for accuracy assessment.

### 3. Results

#### 3.1. Flight Proximity and Nap-of-the-Object Photogrammetry Accuracy

##### 3.1.1. Positioning Accuracy Analysis

The analysis centered on the results obtained at four different flight proximities, as depicted in Table 2. All the images were calibrated with a success rate of 100%. The number of GCPs for each set of flight proximities was nine. The ground resolution value increased from 0.4 cm to 1.2 cm as the flight proximity increased. The mean reprojection error obtained from the four sets of processed data did not differ significantly, remaining stable at approximately 0.012 pixels.

**Table 2.** Processing results for four sets of acquired images.

Processing Parameter	15 m	20 m	25 m	30 m
Number of images	1678	1182	1008	886
Number of calibration images	1678	1182	1008	886
Number of ground control points	9	9	9	9
Ground resolution (cm)	0.4	0.5	0.7	1.2
Mean reprojection error (pixels)	0.010	0.012	0.012	0.014

Four groups of GCP positioning errors obtained at different flight proximities were analyzed as a measure of positioning accuracy. From the results shown in Table 3, it can be seen that the average errors of the GCP coordinates in the X-, Y-, and Z-directions are close to each other with the increase in flight proximity, except for the case of the distance of 30 m. At a flight proximity of 30 m, the average error of the Z-coordinate reaches  $-0.21$  mm. The maximum mean absolute error value, 8.78, occurs in the horizontal direction (x–y coordinates) when the flight proximity is 30 m. In the vertical direction (Z-coordinate), the maximum average error is 7.59 mm when the flight proximity distance is 25 m. In other words, there is not an excessive difference in the average absolute coordinate errors appearing in the three directions.

**Table 3.** Errors of four groups of GCPs.

Flight Proximity (m)	Average Error (mm)			Mean Absolute Error (mm)			Root Mean Square Error (RMSE) (mm)		
	X	Y	Z	X	Y	Z	X	Y	Z
15	0.04	0	-0.12	8.20	6.43	7.27	9.30	8.04	8.15
20	0.05	0.06	-0.07	8.21	7.07	6.76	9.98	8.70	8.11
25	0	0	0.07	8.74	7.40	7.59	9.87	8.77	8.84
30	-0.18	0.15	-0.21	8.78	6.17	7.53	10.40	8.18	8.89

The RMSE of the Z-coordinate decreases and then increases as the flight proximity increases, with a turning point at the flight proximity of 20 m. At a flight proximity of 30 m, the RMSE of the Z-coordinate is the largest, 8.89 mm, and the X-coordinate error value changes the most significantly, reaching a maximum of 10.4 mm. To summarize, the GCP errors are more stable when the flight proximity is 15–20 m.

##### 3.1.2. Point Cloud Reproducibility Analysis

Point cloud data processing is a crucial step in UAV photogrammetry; its outcomes directly impact the overall quality of the results [34]. Four sets of point cloud data, collected at various flight proximities, were imported into PCM V2.0 software and cropped (Figure 8). The cropped point cloud data were denoised and superimposed with the point cloud data generated for the control group (10 m). The mean and variance of the point cloud distances

from the control group were calculated to observe the effects of different flight proximities on the results.

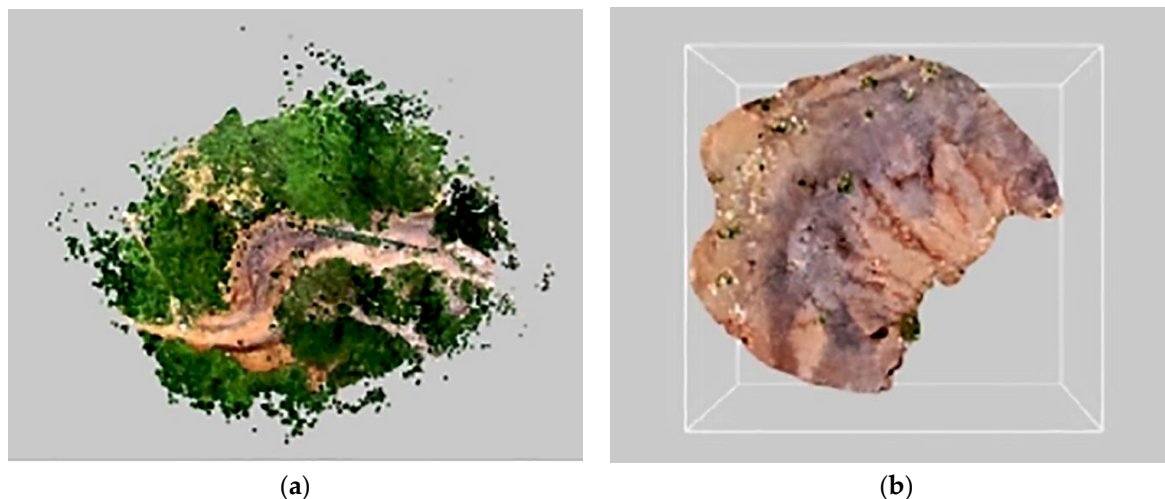


**Figure 8.** (a) Before the point cloud is cropped. (b) After the point cloud is cropped.

The superimposed analysis of the four groups of point cloud data generated at different flight proximities compared with the point cloud data of the control group is illustrated in Figure 9. In terms of distance mean and distance variance, both exhibit an overall upward trend as flight proximity increases. The minimum distance mean and minimum distance variance were observed at a flight proximity of 15 m. Within the flight proximity range of 15–20 m, the overall point cloud superposition distance is closely consistent; when the flight proximity exceeds 20 m, the point cloud distance mean and distance variance both change significantly, reaching 0.175 m and 1.64 m, respectively, at a flight proximity of 30 m. Differences in flight proximity evidently affect the point cloud distance mean and distance variance.

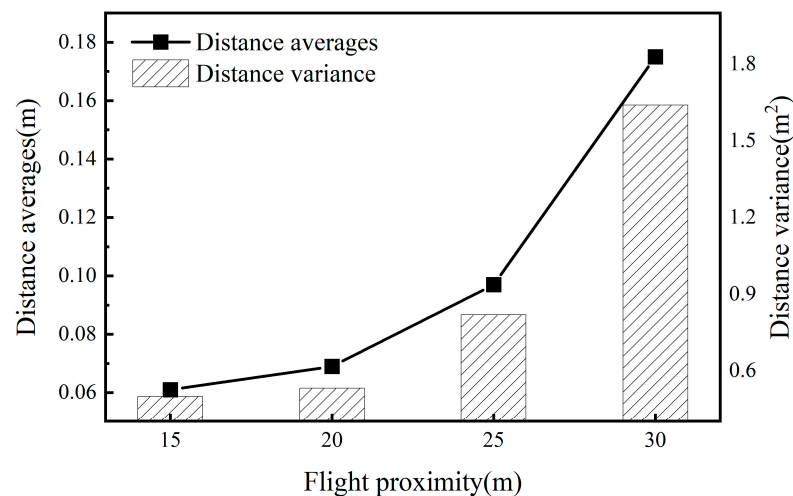


**Figure 9.** Mean and variance results of the distances between the four groups of point cloud data and the control group of point cloud data.

### 3.1.3. DSM Accuracy Analysis

Four sets of image data acquired at different flight proximities were processed to generate DSMs and analyzed with the DSM data generated for the control group (10 m) to explore the relationship between flight proximity and DSM resolution. Figure 10 shows that the DSM resolution decreases gradually as flight proximity increases. There is a close linear correlation between the DSM resolution value and flight proximity ( $R^2 = 0.914$ ).

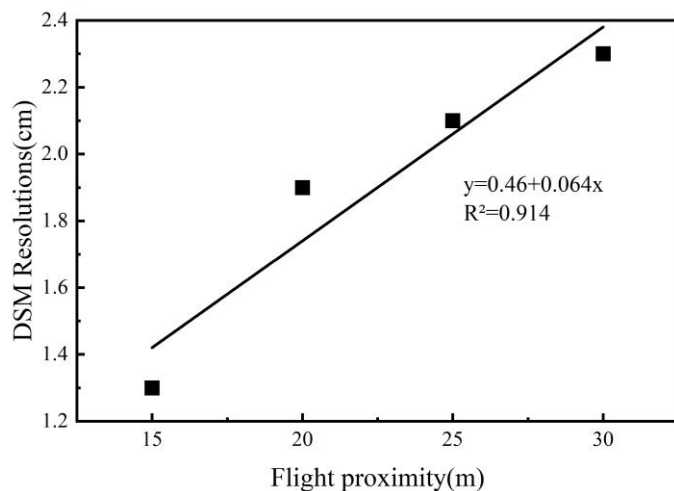


**Figure 10.** Variations in DSM resolution with UAV flight proximity.

Table 4 shows the DSM elevation errors for four sets of flight proximity schemes and the control group at nine GCPs. The highest DSM elevation error value, 0.7 cm, occurs at GCP No. 1 at a flight proximity of 30 m. Among the mean absolute errors of elevation for the nine GCPs, No. 1 has the highest, 0.5 cm; No. 8 has the lowest, only 0.1 cm. The mean absolute elevation error is lower when the flight proximity is 20 m, 0.1, and higher when the flight proximity is 25 m, 0.2 cm. The overall impact of flight proximity on the elevation of the DSM is approximately 0.2 cm.

**Table 4.** Elevation errors of DSMs for experimental groups (cm).

Control Point Number	15 m	20 m	25 m	30 m	Mean Absolute Error
1	0.3	0.3	0.6	0.7	0.5
2	0.1	0.3	0.6	0.5	0.4
3	0.4	0	0	0.1	0.1
4	0.4	0.2	0	0.2	0.2
5	0.3	0.1	0	0.1	0.1
6	0	0.2	0.2	0.1	0.1
7	0.1	0.2	0.5	0.2	0.3
8	0.1	0	0	0.1	0.1
9	0	0.1	0.3	0.1	0.1
Mean absolute error	0.2	0.1	0.2	0.2	0.2

Concerning the resolution of the DSM, the value for the model generated by the control group (10 m) is 1.1 cm. In contrast, the resolution of the DSMs generated for the four different sets of flight proximities shows a minimum value of 1.3 when the flight proximity is 15 m. Therefore, theoretically, the DSM errors between the four sets of data and the control group at the nine GCPs could exceed 1.3 cm. However, as indicated in Table 4, the maximum error is only 0.7 cm.

The DSM data generated from the four sets of data at varying flight proximities were compared against the DSM data from the control group, revealing volume changes among them. Increases would indicate precipitation, and decreases would indicate erosion. Only decreasing volume changes were observed in this case (Figure 11). The volume differences of the four set of data are all below 0.03 m<sup>3</sup>. With flight proximities between 20 m and 25 m, volume changes remain relatively stable at around 0.025 m<sup>3</sup>, suggesting that the DSM data are similar between these two flight proximities. Therefore, combining the positioning accuracy and point cloud data analysis, the flight proximity of 20 m emerges as the optimal scheme for nap-of-the-object photogrammetry in monitoring the Benggang study area.

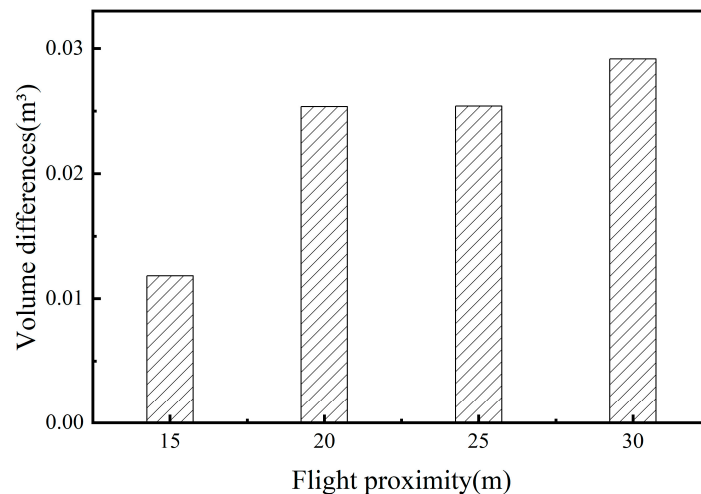


**Figure 11.** Data volume differences of DSMs for all experimental groups.

### 3.2. Accuracy of Control-Free Nap-of-the-Object Photogrammetry Images

#### 3.2.1. DSM Positioning Accuracy

The processing results for images acquired after two phases of the control-free nap-of-the-object photogrammetry image acquisition are shown in Table 5. Both acquisition phases yielded over 1100 images, with 100% completion of in-flight operations and 100% post-data processing image calibration. The average reprojection errors obtained from the two sets of data are similar, both around 0.012 pixels, which is a relatively small value. The DOM image resolution is 5 mm for both phases.

**Table 5.** Basic information of captured images.

Processing Parameter	22 June 2022	15 July 2022
Number of images	1184	1176
Number of dense point clouds	243,626,208	25,329,724
Number of point clouds in the Benggang area	4,412,945	4,534,858
Number of ground checkpoints	10	9
Average reprojection error (pixels)	0.013	0.012
Ground resolution (mm)	5.0	5.0

DSMs were acquired using both image control- and control-free-image-based nap-of-the-object photogrammetry, as shown in Figure 12. Table 6 shows where the accuracy of the DSMs before and after rainfall in both control-free images and image control scenarios is around 0–0.05 m in the X-, Y-, and Z-coordinates. The resolution of the DSMs for both periods is 1.9 cm. The mean absolute errors vary in the planar and vertical directions obtained by the two photogrammetric methods and range from 0.01 to 0.02 m and from 0.01 to 0.03 m, respectively. The mean absolute error and RMSE of X- and Y-coordinates for 06.22 and 07.15 are both 0.01 m. The average error and RMSE in the vertical direction of the Z-coordinate are larger than those of the X- and Y-coordinates. In the vertical Z-coordinate, the absolute average error for both periods is larger than the absolute average error of the image control scenario, with a difference of approximately 0.01 m. The maximum RMSE is 0.03 m, and the minimum is 0.01 m, corresponding to the control-free nap-of-the-object photogrammetry image measurements. The errors between the two periods are small, only 0.01 m and 0.02 m.

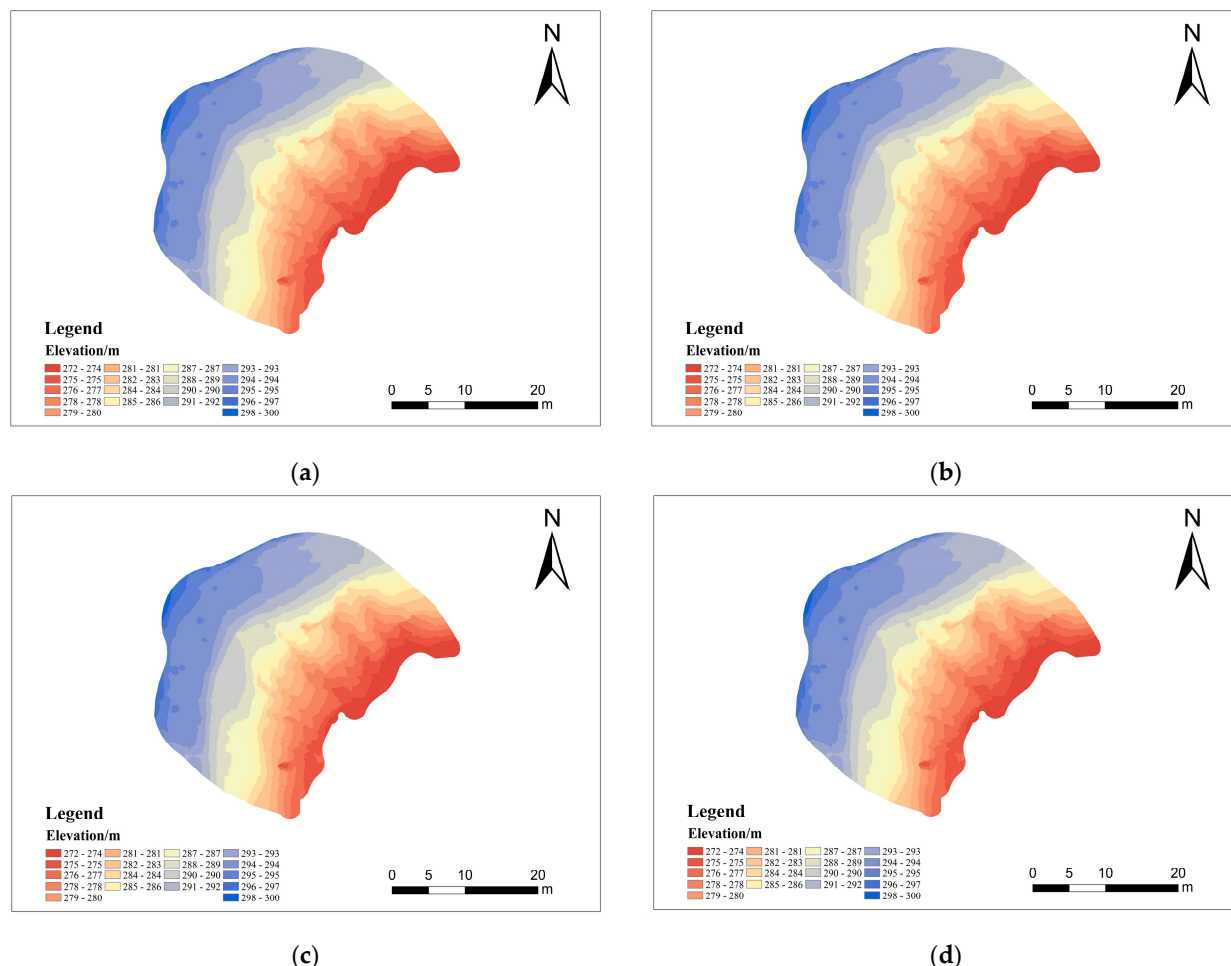


**Figure 12.** DSM data map. (a) 22 June control-free DSM; (b) 22 June image control DSM; (c) 15 July control-free DSM; (d) 15 July image control DSM.

**Table 6.** Results of DSM accuracy analysis for control-free-image and image control cases (unit: m).

Date	CFI or IC	Norm	Ground Checkpoint Name									MAE	RMSE
			1	2	3	4	5	6	7	8	9		
22 June	CFI	$\Delta X$	0.01	0.02	0	0.01	-0.02	0.01	0.01	0.01	0	0.01	0.01
		$\Delta Y$	0	0	-0.01	0.01	0.02	0.01	-0.01	0	0	0.01	0.01
		$\Delta XY$	0.01	0.02	0.01	0.01	0.03	0.01	0.02	0.01	0	0.01	0.02
		$\Delta Z$	0.01	0.01	-0.05	-0.03	-0.03	-0.03	-0.03	-0.03	-0.04	0.03	0.03
	IC	$\Delta X$	0	0.01	0	0.01	-0.02	0.01	0.01	0.01	-0.01	0.01	0.01
		$\Delta Y$	0	0	-0.01	0.01	0.02	0.01	-0.01	0	0	0.01	0.01
		$\Delta XY$	0	0.01	0.01	0.01	0.03	0.01	0.01	0.01	0	0.01	0.01
		$\Delta Z$	0.02	0.01	-0.03	-0.01	-0.01	-0.02	-0.01	-0.01	-0.02	0.02	0.02
15 July	CFI	$\Delta X$	0.01	0.02	0.01	0.01	-0.02	0.01	0.02	0.02	0	0.01	0.01
		$\Delta Y$	-0.01	-0.01	-0.01	0	0.01	0	-0.02	0	0	0.01	0.01
		$\Delta XY$	0.01	0.02	0.01	0.01	0.02	0.01	0.02	0.02	0	0.02	0.02
		$\Delta Z$	0.05	0.05	-0.01	0.01	0.02	0.01	0.02	0.02	0	0.02	0.03
	IC	$\Delta X$	0	0.01	0.01	0.01	-0.02	0.01	0	0.01	-0.01	0.01	0.01
		$\Delta Y$	0	0.01	-0.01	0	0.01	0	-0.01	0	0	0.01	0.01
		$\Delta XY$	0.01	0.01	0.01	0.01	0.02	0.01	0.02	0.01	0.01	0.01	0.01
		$\Delta Z$	0.01	0.01	-0.02	0.01	0.01	0	-0.01	0	-0.01	0.01	0.01

Note: MAE, mean absolute error; RMSE, root mean square error; CFI, control-free image; IC is image control.

In the DSM data, there is strong consistency between the horizontal errors and the vertical errors for the two periods. Horizontal errors are relatively stable, fluctuating around 0.01 m. However, there is a large fluctuation the vertical errors compared with the horizontal errors,

mainly due to the larger error values of ground checkpoints No. 2 and No. 3. The main factor affecting the accuracy is that checkpoints No. 2 and No. 3 were located at the bottom and top of the study area, respectively, where the 3D point error was significant. The UAV control-free nap-of-the-object photogrammetry technology demonstrates high positioning accuracy in terms of DSMs, with the error reaching the subcentimeter level.

The 2D error kernel density distribution was plotted based on the planimetric and elevation errors of the DSMs generated by control-free nap-of-the-object photogrammetry images, as shown in Figure 13. The elevation error for 22 June is mainly concentrated in the range of  $-0.02$  to  $-0.04$  m, and the planar direction error is mainly concentrated around 0.1 m. The elevation error for 15 July is mainly concentrated around 0.02 m, and the planar direction error is mainly concentrated between 0.01 m and 0.02 m.

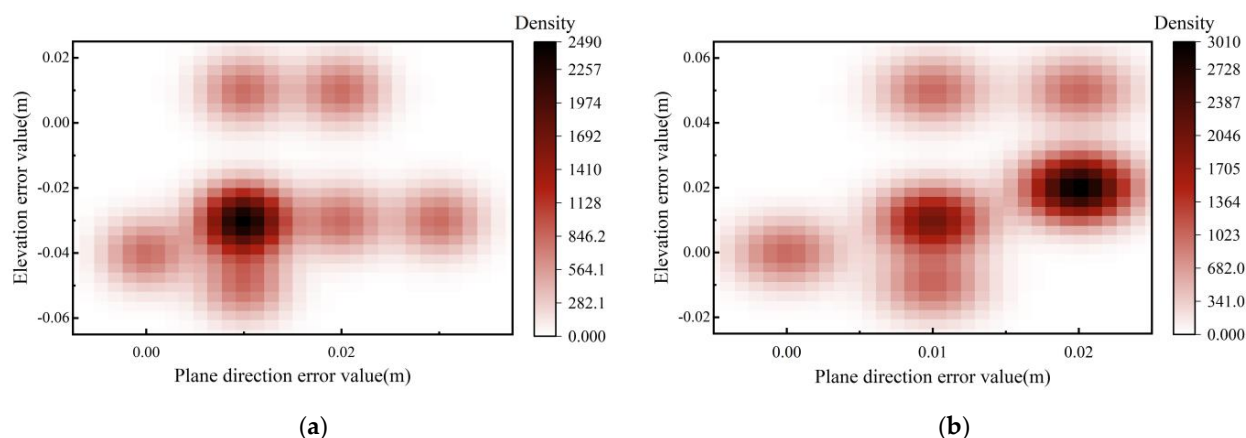


**Figure 13.** Error kernel density plots. (a) 22 June; (b) 15 July.

### 3.2.2. Measurement Error of DSMs

The data collected via image control nap-of-the-object photogrammetry were used as a reference to determine the measurement accuracy of DSM data obtained through control-free-image-based nap-of-the-object photogrammetry. The image data collected in different sessions (22 June and 15 July 2022) were individually processed, generating mean absolute error and standard deviation information for the DSM data of the two periods, as depicted in Figure 14. From the figure, we can see a gradual increase in the mean absolute error and standard error of DSM data for the two periods, before and after rainfall. However, the maximum mean absolute error in the DSM with or without image control points, before and after rainfall, is only 0.031 m (i.e., relatively small).

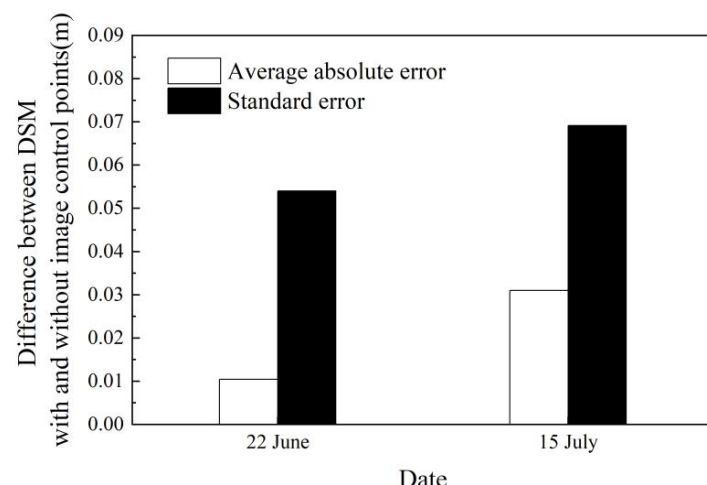


**Figure 14.** Difference diagrams of DSMs with and without image control points.

The DSM was utilized to generate profiles of the erosion gully along the X- and Y-directions. Line 1 represents the cross-section along the X-direction, and Line 2 is the cross-section along the Y-direction of the erosion gully (Figure 15). Data from the two periods before and after rainfall were used to extract profiles of the erosion gully for both periods, as depicted in Figure 16.

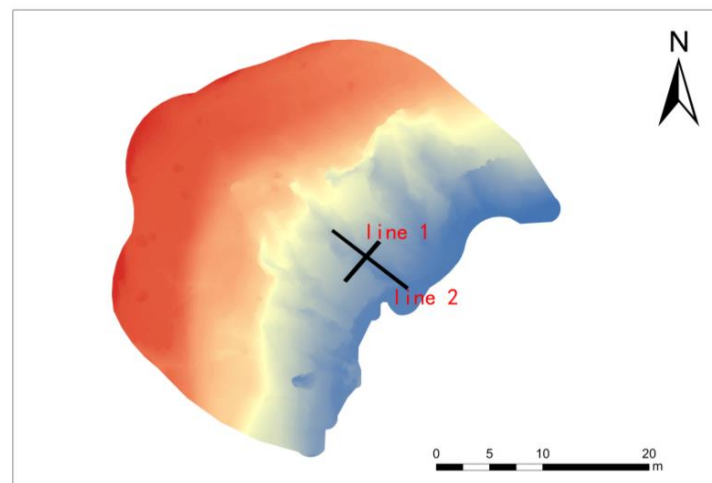


**Figure 15.** Profile line bitmap of DSM with and without image control points.

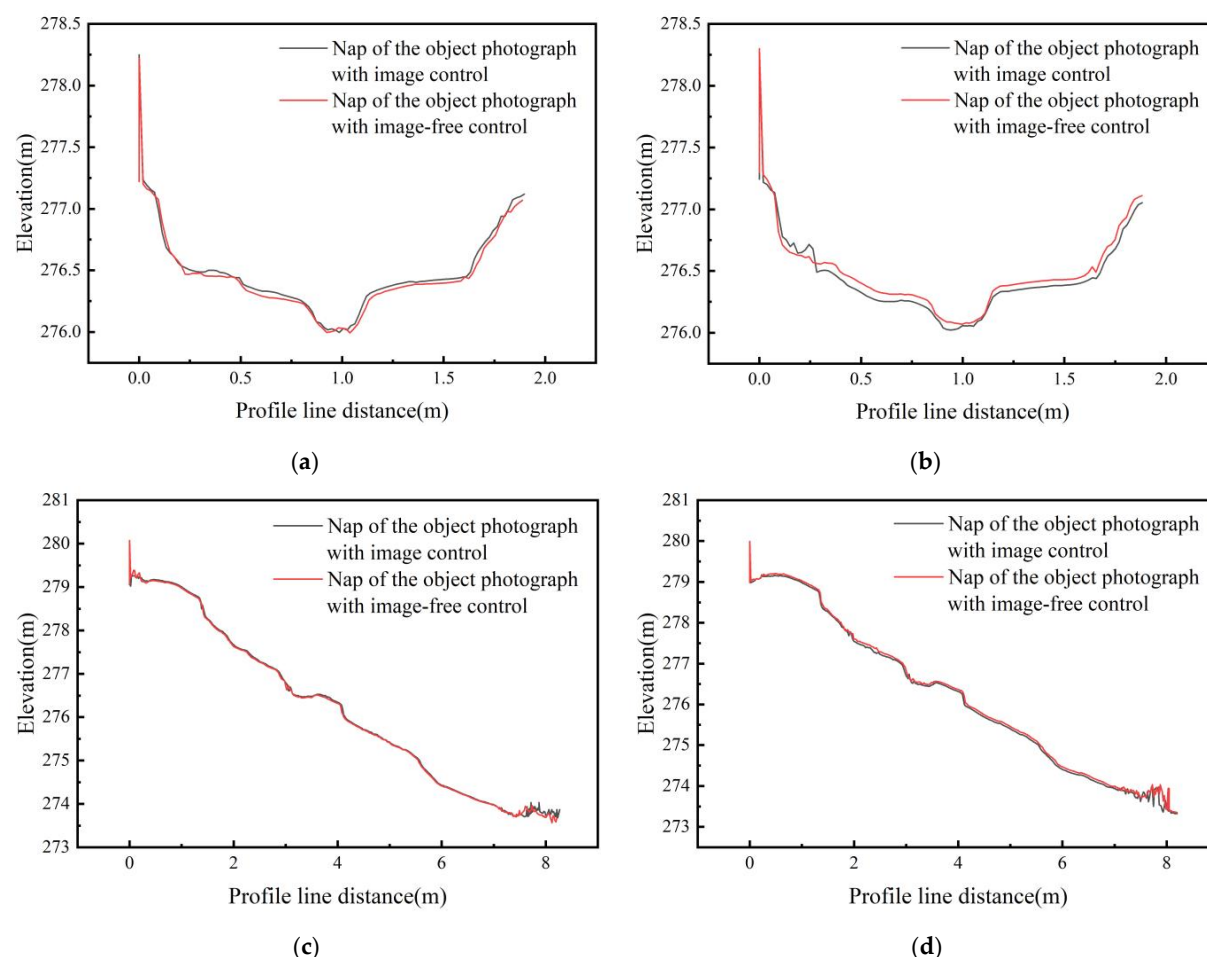


**Figure 16.** Profile of DSM with and without image control points. (a) 22 June Line 1 DSM profile; (b) 15 July Line 1 DSM profile; (c) 22 June Line 2 DSM profile; (d) 15 July Line 2 DSM profile.

The profile analysis of Line 1 reveals a consistent trend in the profiles obtained with or without image control points before and after rainfall. A similar trend is observable in the profile of Line 2, indicating a high degree of coincidence. However, there is a significant fluctuation in the section distance from 7.5 mcm to 8.5 m. The average height error for 22 June is approximately 6.94 cm, with an offset along the X-axis of approximately 11.78 cm. For 15 July, the average height error is around 5.02 cm, with an offset along the X-axis of about 6.41 cm. However, the deviation in elevation and X-direction observations for both periods remains at the subcentimeter level.

#### 4. Discussion

##### 4.1. Reliability of Control-Free Nap-of-the-Object Photogrammetry Technique

In previous research on Benggang erosion monitoring by UAV photogrammetry, most study areas were performed in regions with highly complex topography [8,9,15]. The traditional method of establishing image control points is excessively time-consuming, labor-intensive, and challenging in terms of field operations [13,14,16]. Though the accuracy achieved by UAV measurement coupled with GNSS RTK technology can fall below the centimeter level, it necessitates manually navigating hazardous terrain [35].

In this study, control-free-image-based nap-of-the-object photogrammetry technology was applied to measure Benggang erosion. The positioning and measurement accuracy errors of the obtained DSMs all reached the subcentimeter level. The planar direction error was mainly concentrated between 0.01 m and 0.02 m, which is consistent with results for seismogenic faults measured via orthophotography, as discussed by Liu et al. [36]. In this study, nap-of-the-object photogrammetry was found to reduce the accuracy error through multi-angle and close-distance photography compared with orthophotography in a single direction. The relatively low altitude of the UAV also allowed for more accurate data acquisition.

The combination of UAV control-free nap-of-the-object photogrammetry and geological monitoring, as evaluated by Zhou et al. [25] in the context of debris flow disasters, aligns with the results of the present study. However, the accuracy of the results in terms of planar and elevation errors surpasses that achieved by Zhou et al. [25]. This improvement can be attributed to the control-free images attained through nap-of-the-object photogrammetry, which, in contrast to the oblique photography employed in the aforementioned study, results in a more refined system capable of reducing errors in DOM images and DSMs. In summary, the results of this analysis demonstrate that control-free nap-of-the-object photogrammetry imaging is well suited to the measurement of Benggang erosion.

##### 4.2. Advantages of Control-Free Nap-of-the-Object Photogrammetry

Based on the results of image processing with and without image control, a comparative analysis was conducted on the 22 June data obtained with the two photogrammetry methods. This analysis centered on image data acquisition and indoor data processing efficiency.

In terms of data acquisition, control-free-image-based nap-of-the-object photogrammetry appears to be a straightforward, rapid, and efficient approach for obtaining image data. The equipment required only includes a UAV and flight planning software; the entire process can be executed by a single individual. Conversely, the image control technique necessitates additional equipment for ground image control points, in addition to the advance surveying of the study area for the strategic placement of these points. This method involves at least two or more personnel; therefore, it is more labor-intensive and time-consuming.

Concerning image data processing, the process primarily comprises four steps: CGP marking, Encryption processing of aerial triangulation, DOM image processing, and DSM processing. Figure 17 illustrates the two photogrammetric processing workflows, with the specific processing times detailed in Table 7. The time required for the control-free technique is markedly less than that for the image control technique, ranging from 283.84 to 216.58 min. The DSM processing step demands the most time among the four steps, ranging from 180.05 min to 190.93 min. The complexity and technical demands of image control processing contribute to the technique's extended duration, especially in terms of control

point marking, which must be meticulously executed to ensure sufficient precision. The intricate nature of this process precludes full automation, thereby increasing the workload for processing.

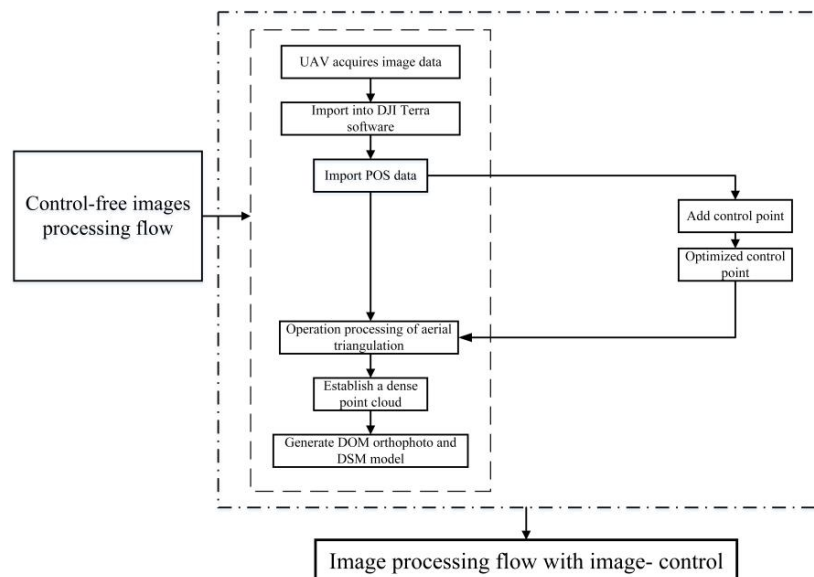


**Figure 17.** Image processing flow chart with and without image control points.

**Table 7.** Internal image data processing with and without image control points (min).

With or Without Image Control	Control Point Marker	Aerial Triangulation Processing Time	DOM Image Processing	DSM Processing	Total
Image control	58.00	13.91	21.00	190.93	283.84
Control-free images	/	15.88	20.65	180.05	216.58

Image control nap-of-the-object photogrammetry required the longest processing time among the photogrammetry methods compared in this study, 283.84 min. Control-free-image-based nap-of-the-object photogrammetry required only 216.58 min, representing the fastest processing efficiency. Control-free image data can be processed swiftly and straightforwardly with a high degree of automation. The efficiency in obtaining DOM images and DSMs is significant, streamlining the indoor processing workflow. Utilizing this technique with UAVs in the Benggang study area would facilitate close observations of the Benggang surface, yielding high-quality image data that meet the standards of fine millimeter modeling. Further, this approach would enhance the accuracy of monitoring dynamic Benggang changes pre- and post-rainfall.

As a novel aerial survey technology, control-free-image-based nap-of-the-object photogrammetry satisfies relevant requirements in precision, non-contact operation, penetration, and rapidity, making it potentially broadly applicable. Nevertheless, in actual monitoring scenarios, it is currently limited to relatively small areas and exhibits other notable constraints. While this technology excels at capturing details of collapse walls at close range, considerations regarding safe distances limit the accurate depiction of deeper gullies. Moreover, the significant terrain drop in large-scale Benggang poses challenges in maintaining stable elevation errors in the 3D model. Further research is warranted to address the planar and elevation error challenges inherent to complex 3D models of large-scale Benggang landscapes.

## 5. Conclusions

This study focuses on the Benggang of Tongluo Mountain in Longmen Town, Anxi County, Fujian Province, to explore the application of control-free-image-based nap-of-the-

object photogrammetry for dynamic erosion monitoring. The aim is to develop an innovative technique for advancing Benggang erosion monitoring processes. The key findings can be summarized as follows:

- (1) The resolution of DSMs gradually increases with a robust linear correlation ( $R^2 = 0.914$ ) over the course of the analysis. Considering positioning accuracy, point cloud data, and DSM analysis, the flight proximity distance of 20 m emerges as the optimal scheme for nap-of-the-object photogrammetry to obtain data in the Benggang study area.
- (2) The average reprojection errors for nap-of-the-object photogrammetry with and without image control do not differ significantly, both approximating 0.012 pixels. There is no significant difference between the two photogrammetry methods in the positioning accuracy of the DSMs in the planar and vertical directions, which resulted to be about 0.01 m and 0.03 m, respectively. The error analysis of the DSMs indicates a consistent trend in the profiles obtained with and without image control points before and after rainfall. Moreover, the elevation errors along the X- and Y-axes are less than 6.94 cm and 11.78 cm, respectively. Notably, both elevation and X-axis errors fall within the subcentimeter range.

In conclusion, control-free-image-based nap-of-the-object photogrammetry technology proves capable of meeting the monitoring requirements of Benggang erosional areas. It can provide valuable technical support for large-scale, safe, and efficient erosion monitoring efforts.

**Author Contributions:** Conceptualization, L.Z.; Methodology, L.Z. and Y.Z.; Software, L.Z. and G.L.; Validation, J.L. (Jinshi Lin); Formal analysis, X.J.; Investigation, L.Z.; Data curation, L.Z. and J.L. (Jianfeng Lai); Writing—original draft, L.Z.; Writing—review & editing, J.L. (Jinshi Lin); Supervision, J.L. (Jinshi Lin); Project administration, F.J. and Y.H. All authors have read and agreed to the published version of the manuscript.

**Funding:** This work was supported by the Water Conservancy Science and Technology Project of Fujian Province (KJG21009A) and the Significant Science And Technology Projects of the Ministry of Water Resources (SKS-2022073).

**Institutional Review Board Statement:** Not applicable.

**Informed Consent Statement:** Not applicable.

**Data Availability Statement:** The raw data supporting the conclusions of this article will be made available by the authors on request.

**Conflicts of Interest:** The authors declare no conflict of interest.

## References

1. Liao, Y.; Yuan, Z.; Zhuo, M.; Huang, B.; Nie, X.; Xie, Z.; Tang, C.; Li, D. Coupling effects of erosion and surface roughness on colluvial deposits under continuous rainfall. *Soil Tillage Res.* **2019**, *191*, 98–107. [[CrossRef](#)]
2. Jiang, F.; Huang, Y.; Wang, M.; Lin, J.; Zhao, G.; Ge, H. Effects of Rainfall Intensity and Slope Gradient on Steep Colluvial Deposit Erosion in Southeast China. *Soil Sci. Soc. Am. J.* **2014**, *78*, 1741–1752. [[CrossRef](#)]
3. Deng, Y.; Xia, D.; Cai, C.; Ding, S. Effects of land uses on soil physic-chemical properties and erodibility in collapsing-gully alluvial fan of Anxi County, China. *J. Integr. Agric.* **2015**, *15*, 1863–1873. [[CrossRef](#)]
4. Xu, J. Benggang erosion: The influencing factors. *Catena* **1996**, *27*, 249–263.
5. Zhang, X. The practice and prospect of hill collapsing improving and development in southern China. *China Water Resour.* **2010**, *4*, 17–18+22.
6. Woo, M.; Fang, G.; diCenzo, P.D. The role of vegetation in the retardation of rill erosion. *Catena* **1997**, *29*, 145–159. [[CrossRef](#)]
7. Zhu, X.; Gao, L.; Wei, X.; Li, T.; Shao, M. Progress and prospect of studies of Benggang erosion in southern China. *Geoderma* **2023**, *438*. [[CrossRef](#)]
8. Liao, Y.; Yuan, Z.; Li, D.; Zheng, M.; Huang, B.; Xie, Z.; Wu, X.; Luo, X. What kind of gully can develop into benggang? *Catena* **2023**, *225*, 107024. [[CrossRef](#)]
9. Liu, X.; Zhang, D. Temporal-spatial analyses of collapsed gully erosion based on three-dimensional laser scanning. *Editor. Off. Trans. Chin. Soc. Agric. Eng.* **2015**, *31*, 204–211.
10. Shen, S.; Chen, J.; Zhang, S.; Cheng, D.; Wang, Z.; Zhang, T. Deep Fusion of DOM and DSM Features for Benggang Discovery. *ISPRS Int. J. Geo-Inf.* **2021**, *10*, 556. [[CrossRef](#)]

11. Neugirg, F.; Stark, M.; Kaiser, A.; Vlacičová, M.; Seta, M.D.; Vergari, F.; Schmidt, J.; Becht, M.; Haas, F. Erosion processes in calanchi in the Upper Orcia Valley, Southern Tuscany, Italy based on multitemporal high-resolution terrestrial LiDAR and UAV surveys. *Geomorphology* **2016**, *269*, 8–22. [[CrossRef](#)]
12. Han, Y.; Oh, H.J. RNCC-based Fine Co-registration of Multi-temporal RapidEye Satellite Imagery. *J. Korean Soc. Surv. Geod. Photogramm. Cartogr.* **2018**, *36*, 581–588.
13. Jiang, X.; Liang, Z.; Zhou, H.; Dai, Y.; Chen, Y. Dynamic Change Monitoring of Collapse Based on UAV Oblique Photograph Technique. *Trop. Geogr.* **2019**, *39*, 597–603.
14. Zhou, X.; Yu, H.; Wei, Y.; Hu, J.; Cai, C. Method for monitoring change in Benggang erosion based on oblique aerial images of UAV. *J. Agric. Eng.* **2019**, *35*, 51–59.
15. Ren, B.; Ding, S.; Wu, D.; Li, S. Study of headward erosion characteristics of collapsed downland in granite region in southeast Hubei Province. *People's Chang.* **2015**, *46*, 76–79.
16. Li, Z.; Zhong, L.; Huang, Y.; Ge, H.; Zhu, Y.; Jiang, F.; Li, X.; Zhang, Y.; Lin, J. Monitoring technology for collapse erosion based on the nap of the object photograph of UAV. *Editor. Off. Trans. Chin. Soc. Agric. Eng.* **2021**, *37*, 151–159.
17. Zhang, Z. *Origin and Meaning of Nap of the Object Photograph*; Wuhan University, School of Remote Sensing Information Engineering: Wuhan, China, 2019.
18. Zhang, Z.; Tao, P. An Overview on “Could Control” Photogrammetry in Big Data Era. *J. Surv. Mapp.* **2017**, *46*, 1238–1248.
19. Liang, J.; Tie, Y.; Zhao, C.; Zhang, X. Technology and method research on the early detection of high-level collapse based on the Nap-of-the-object photography. *Geol. Surv. China* **2020**, *7*, 107–113.
20. Li, C.; Zhang, G.; Lei, T.; Gong, A. Quick image-processing method of UAV without control points data in earthquake disaster area. *Trans. Nonferrous Met. Soc. China* **2011**, *21*, s523–s528. [[CrossRef](#)]
21. Zhao, H.; Gou, Z.; Gao, P.; Cheng, Y. No ground control point making the orthophoto for the UAV remote sensing system. In *International Symposium on Photoelectronic Detection and Imaging 2007: Related Technologies and Applications*; Society of Photo Optical: Bellingham, WA, USA, 2008.
22. He, H.; Chen, T.; Zeng, H.; Huang, S. Ground Control Point-Free Unmanned Aerial Vehicle-Based Photogrammetry for Volume Estimation of Stockpiles Carried on Barges. *Sensors* **2019**, *19*, 3534. [[CrossRef](#)] [[PubMed](#)]
23. Li, X.; Xiong, B.; Yuan, Z.; He, K.; Liu, X.; Liu, Z.; Shen, Z. Evaluating the Potentiality of Using Control-free Images from a Mini Unmanned Aerial Vehicle (UAV) and Structure-from-Motion (SfM) Photogrammetry to Measure Paleoseismic Offsets. *Int. J. Remote Sens.* **2021**, *42*, 2417–2439. [[CrossRef](#)]
24. Maier, K.; Nascetti, A.; Van Pelt, W.; Rosqvist, G. Direct photogrammetry with multispectral imagery for UAV-based snow depth estimation. *ISPRS J. Photogramm. Remote Sens.* **2022**, *186*, 1–18. [[CrossRef](#)]
25. Zhou, X.; Jia, Q.; Shi, P.; Guo, B.; He, F.; He, W.; Li, P. Application of image-free control UAV aerial survey technology in emergency treatment of landslide-debris flow disaster in Lijie north hill, Zhouqu County. *Chin. J. Geol. Hazard Control* **2022**, *33*, 107–116.
26. Wu, J.; Wang, P.; Wang, J.; Wu, X.; Su, X. Low Altitude Photogrammetry of Sea Islands and Reefs without Ground Control Points: Research and Application. *J. Yangtze River Sci. Res. Inst.* **2022**, *39*, 133–137.
27. Chudley, T.R.; Christoffersen, P.; Doyle, S.H.; Abellán, A.; Snooke, N. High-accuracy UAV photogrammetry of ice sheet dynamics with no ground control. *Cryosphere* **2019**, *13*, 955–968. [[CrossRef](#)]
28. Wu, H.; Zhang, X. Optimization Study of Laying Scheme of Image Control Points in UAV Low Aero Photogrammetry. *Surv. Sci. Technol.* **2018**, *12*–15.
29. Su, S.; Wang, Y. Control points layout for the precision of aerial survey. *Sci. Surv. Mapp.* **2012**, *37*, 115–117.
30. Xie, D.; Hu, R.; Wang, C.; Zhu, C.; Xu, H.; Li, Q. A Simulation Framework of Unmanned Aerial Vehicles Route Planning Design and Validation for Landslide Monitoring. *Remote Sens.* **2023**, *15*, 5758. [[CrossRef](#)]
31. Lin, Z.; Xie, F.; Su, G. Accuracy Analysis of Low Altitude Photogrammetry with Wide-angle Camera. *Acta Geod. Cartogr. Sin.* **2014**, *43*, 991.
32. Zhou, J.; Gong, J.; Liu, W. Application of UAV Close-in Photogrammetry in Landside Monitoring. *Ceomatics Spat. Inf. Technol.* **2023**, *46*, 183–189.
33. Yang, B.; Pang, Z.; Wen, W. Research on the application of nap of the object photogrammetry technology in 3D real scene modeling of ancient architecture. *Stand. Surv. Mapp.* **2023**, *39*, 110–114.
34. Fazeli, H.; Samadzadegan, F.; Dadrasjavan, F. *Evaluating the Potential of RTK-UAV for Automatic Point Cloud Generation in 3D Rapid Mapping*; Copernicus GmbH: Göttingen, Germany, 2016.
35. Du, Y.; Li, S.; Ding, S.; He, Y.; Deng, Y. Study of CORS–RTK combined with GIS in collapsing gully monitoring of southeast Hubei Province. *Yangtze River* **2015**, *46*, 87–90.
36. Liu, C.; Wang, Y.; Yu, S.; Lei, Q.; Yang, S. Positioning Accuracy Analysis of the New Portable Industry-level Unmanned Aerial Vehicle Phantom 4RTK. *Technol. Earthq. Disaster Prev.* **2022**, *17*, 114–123.

**Disclaimer/Publisher’s Note:** The statements, opinions and data contained in all publications are solely those of the individual author(s) and contributor(s) and not of MDPI and/or the editor(s). MDPI and/or the editor(s) disclaim responsibility for any injury to people or property resulting from any ideas, methods, instructions or products referred to in the content.